Highlights

Oxygen Vacancy Effects in the Electronic and Magnetic Structure of $La_{0.7}Sr_{0.3}MnO_3$ Epitaxial Thin Films from First Principles

Zachary Romestan, Xu He, A. C. Garcia-Castro, Navid Mottaghi, Mikel Holcomb, Aldo H. Romero

- Oxygen vacancies near the LSMO/STO interface redistribute charge to low spin configurations.
- Low spin configurations result in magnetization deterioration.
- Oxygen acancies cause competing super-exchange via charge redistribution.

Oxygen Vacancy Effects in the Electronic and Magnetic Structure of $La_{0.7}Sr_{0.3}MnO_3$ Epitaxial Thin Films from First Principles

Zachary Romestan[a,*], Xu He[b], A. C. Garcia-Castro[c], Navid Mottaghi[a],
Mikel Holcomb[a], Aldo H. Romero[a]

[a] *Department of Physics, West Virginia University, 135 Willey Street, Morgantown, 26506, WV, United States*
[b] *Catalan Institute of Nanoscience and Nanotechnology (ICN2), CSIC, BIST, Campus UAB, Bellaterra, Barcelona, 08193, Spain*
[c] *School of Physics, Universidad Industrial de Santander, Bucaramanga, 680002, Colombia*

Abstract

$La_{0.7}Sr_{0.3}MnO_3$ (LSMO) is a promising material for spintronic applications due to its robust ferromagnetism and complete spin polarization. However, these properties are known to degrade in thin films. Oxygen vacancies are believed to be a critical factor in this degradation, but experimentally isolating their effects has proven challenging. In this work, we use first-principles calculations to theoretically investigate how oxygen vacancies affect the magnetic structure of LSMO thin films. Our results reveal that oxygen vacancies act as scattering centers, leading to charge redistribution within the bulk layers. This redistribution disrupts the ferromagnetic double-exchange interaction and introduces competing

---

[*] Corresponding author
Email addresses: `zlromestan@mix.wvu.edu` (Zachary Romestan), `mailhexu@gmail.com` (Xu He), `acgarcia@saber.uis.edu.co` (A. C. Garcia-Castro), `mottaghi.navid@gmail.com` (Navid Mottaghi), `mikel.holcomb@mail.wvu.edu` (Mikel Holcomb), `Aldo.Romero@mail.wvu.edu` (Aldo H. Romero)

Preprint submitted to Journal of Alloys and Compounds *November 12, 2024*

super-exchange interactions, causing local spin flipping and ultimately reducing the overall magnetization.

Keywords: Manganites, Vacancies, Half-metals, Local DOS, DFT, Exchange Interactions

---

1. Introduction

Rare earth manganites of the form RMnO$_3$ (R = rare earth) have been a focal point of materials design for decades due to their exceptional sensitivity to cation substitution **? ? ?**]. In particular, the La$_x$Sr$_{1-x}$MnO$_3$ family exhibits colossal magnetoresistance (CMR), orbital order, multiple charge ordered phases, magnetic transitions, and metal-insulator transitions by varying the Sr content **? ? ?**]. The rich physics that results from cation substitution is enticing for applications in magnetic tunnel junctions **?**], solid oxide fuel cells **?**], and memristors **?**]. While SrMnO$_3$ and LaMnO$_3$ are both antiferromagnetic (AFM) insulators at room temperature **? ? ?**], the alloys become ferromagnetic (FM) with metallic and half-metallic behavior for $0.1 \leq x \leq 0.5$ **?**] through the double exchange interaction. La$_{0.7}$Sr$_{0.3}$MnO$_3$ (LSMO) is exceptional due to its large magnetic moment, complete spin-polarization at the Fermi level, Curie point above room temperature **?**], and highly efficient CMR **?**]. These properties make LSMO an excellent candidate for spintronic device applications. These applications necessitate reduced dimensionality, but the magnetic properties of thin films are found to deviate from their bulk counterparts **? ? ?**]. In LSMO the reduction of film thickness **?**] leads to magnetic deterioration at the film surface, known as the magnetic dead layer (MDL). In addition to the MDL, there is further evidence that demonstrates a variety of complex magnetic phenomena in manganites such as interfacial dead layers **?**], competing magnetic domains **? ?**], and spontaneous magnetic reversal **? ?**] as a consequence of the reduced dimensionality. Likewise, the electrical conductivity degrades with film thickness **? ?**] which further hinders potential developments based on LSMO. Property degradation is well documented, but there is no global consensus on the precise underlying mechanisms that are responsible. While the dependence on film thickness is clear, the reduction of dimensionality invites the consideration of new degrees of freedom, such as epitaxial strain **?**], interfacial charge redistribution **? ? ?**], and point defects **? ?**], that might increasingly influence the material properties and performance as thin-films thickness is reduced. As each of these occur simultaneously, discerning the mechanism is ambiguous. Oxygen vacancies are believed to play a crucial role, as evidence suggests they significantly impact the magnetic and electronic properties of (La,Sr)MnO_3 materials **?**].

In this work, we carefully investigate the effects that oxygen vacancies have on the magnetic and electronic structure of LSMO thin-films. We introduce oxygen vacancies into our theoretical modeling of LSMO/STO thin films in order to unveil and understand the key features relative to experimental findings. From the oxygen-deficient thin film models, we are able to reproduce the formation of magnetic dead layers near the surfaces. Additionally, we find further magnetization degradation throughought caused by the redistribution of charge induced by the presence of vacancies.

2. Computational and Theoretical Methods

To study the effects of oxygen vacancies in bulk LSMO we employed first principles calculations within Density Functional Theory **? ?**] (DFT) as it is implemented in VASP **? ?**] (version 5.4.4), using the PAW method **?**]. The exchange correlation functional was approximated with the PBEsol **?**] GGA exchange-correlation functional, and the plane wave basis was expanded up to a cutoff of 600 eV to ensure accurate total energies and forces. The pseudopoentials included 11 electrons from La, 10 from Sr, 13 from Mn, and 6 from O with the electronic configurations of La:$5s^2 5p^6 5d^1 6s^2$ (version La 06Sep2000), Sr:$4s^2 4p^6 5s^2$ (version Sr_{sv} 07Sep2000), Mn:$3p^6 4s^2 3d^5$ (version Mn_{pv} 02Aug2007), and O:$2s^2 2p^4$ (version O 08Apr2002). To account for the localization of the Mn d-electrons we used the LDA+U correction within the Liechtenstein **?**] formalism for the Mn $3d$ elections, setting U to a value of 2.7 eV and J to a value of 1.0 eV. The Sr content was modeled using the Virtual Crystal Approximation **?**] (VCA). The chosen value for (J, U) in combination with the VCA treatment that we use in this study has been shown to arrive at results that are consistent with experimental measurements in our prior work **?**]. Likewise, in the present study we reproduce the expected half-metal electronic structure. Utilizing VCA, the effects of the OV are isolated from the effects of the Sr ordering. Within the 20 atom unit cell the Brillouin zone was sampled using a $6 \times 6 \times 4$ Monkhorst-Pack mesh grid. The thin film structure consists of 5 cubic layers of $\mathrm{SrTiO_3}$ (STO), where we have fixed the first layer of the substrate to simulate the bulk. The remaining 4 layers of STO and all of the layers of $\mathrm{La_{0.7}Sr_{0.3}MnO_3}$ (LSMO) were allowed to freely relax. On top of the 5 layers of STO, we placed 8 layers of LSMO. To avoid artificial effects caused by the interaction with periodic images, we have added a 16 Å vacuum above the LSMO surface. The geometries were optimized with respect to the cell parameters, cell volume and ionic positions until the interatomic forces were converged below 10^{-4} eV/Å.

The OV formation energy ΔE was calculated as

$$\Delta E = E_v + \mu_O - E_p \tag{1}$$

where E_v is the DFT total energy of the unit cell containing vacancies, E_p is the DFT total energy of the corresponding pristine structure and μ_O is the chemical potential of oxygen. μ_O was taken to be half of the DFT total energy for the oxygen dimer. The systems considered in this work are not within the diffuse limit, therefore the calculated formations energies are not equivalent to the amount of energy needed to create a vacancy. Rather, we chose to model the effects of vacancy clusters that may form in physical samples, where the formation energy informs the relative stability of each system.

To understand the first principles results for the magnetic structure of these systems, the magnetic exchange coupling parameters were calculated from the Heisenberg Hamiltonian, written as

$$E = -\sum_{ij,i\neq j} J_{ij}\mathbf{S}_i \cdot \mathbf{S}_j \tag{2}$$

where each $\mathbf{S}_i$ is normalized to 1. The exchange parameters were calculated using the TB2J **?**] python package, which calculates the exchange integrals directly from a projected tight-binding Hamiltonian **?** **?**]. We used Wannier90 **?**] to create the tight-binding model where the Kohn-Sham orbitals were projected over Wannier functions for the (La,Sr) d-orbitals, Mn d-orbitals, and O p-orbitals. Projections were considered to be maximally localized when the difference of the spread functional between iterations was less than 10^{-10}. The maximally localized Wannier functions were then used to calculate the exchange interactions between Mn ions.

3. Results and Discussion

3.1. Structural features:

The four oxygen-deficient heterostructures were created by separately introducing a single oxygen vacancy in each of the four positions of the pristine slab as highlighted in Fig. 1. In each case, the in-plane lattice parameter was fixed to the bulk value of the STO substrate, imposing a tensile strain of +1.7% to match experimental conditions near the interface. The internal coordinates were allowed to relax, but the volume of the cell was constrained to retain the added vacuum. In this procedure, we see the layer-by-layer variation of the pseudocubic c lattice parameter as a function of the vacancy position. The theoretically obtained layer-by-layer profiles, shown in Fig. 2, contain three distinct regions for all of the heterostructures. These regions are the behaviors of the STO parameter just before the interface, the pronounced expansion seen at the interface, and the relaxation behavior of the LSMO moving towards the surface.

The expansion seen at the interface is often reported in perovskite thin films. Frequently, the peak is attributed to oxygen vacancy formation at the interface **?**] as a response to the strain caused by the lattice mismatch. However, this assumes a purely elastic response to strain. In perovskites, elastic lattice distortions are indeed a stress compensation mechanism, but the coordination network offers additional degrees of freedom to respond to the interfacial stress. For example, the O-Mn-O bonding chains may buckle or straighten, modifying the rigid octahedral tilting. The additional degrees of freedom can serve as a so-called symmetry compensation **?**] mechanism that has been observed in LSMO/STO thin films, where the LSMO octahedral tilts are suppressed and the STO octahedra gain tilting in order to match the symmetry at the interface. This results in an out-of-plane (OOP) expansion accompanied by a reduction in the substrate parameter just before the interface in a manner that is similar to what we observe in our models. Although this expansion is frequently attributed to vacancies near the interface, we find that the expansion also occurs for the pristine LSMO model film as shown in Fig. 2. In fact, the position of a vacancy in our heterostructures has no appreciable effect on the interfacial peak unless the vacancy occurs in an Mn-O-Ti bonding chain across the interface. In this instance, the interface expansion nominally increases by 0.05 Å and suppresses the dip in the STO parameter that is seen in the other cases. Therefore, we find that the interfacial expansion is a general property of the LSMO/STO interface that results from symmetry compensation which is independent of vacancy formation.

On the other hand, the location of the vacancy does impact the relaxation of the lattice parameter into the bulk of the LSMO sample as shown in Fig. 2. Vacancies near the interface show a reduction in the lattice parameter from that of bulk LSMO. The vacancies away from the interface result in local expansion of the lattice parameter from that of bulk LSMO. Lattice parameter expansion that has been observed in X-ray diffraction experiments **?**] has been correlated with delocalization of the excess electrons from the vacancies and weakening of the Mn bonding covalency which leads to increased Mn-Mn distance in the presence of vacancies **?**]. Recent first-principles work indicates that localization of the excess electrons in occupied defect states is correlated with the shortening of the Mn-Mn distance **?**]. In Fig. S1, we present the layer-by-layer density of states for each of the thin film models with vacancies. We find sharply localized defect levels below the Fermi energy for vacancies near the interface and the absence of occupied defect levels for vacancies away from the interface. This correlation between the lattice parameter and the presence of occupied defect levels indicates that the proximity of vacancies to the interface influences the localization of the excess electrons.

3.2. Magnetization and Dead Layer:

We find a total magnetization of 3.06 μ_B per Mn for the pristine model film. Despite the vacancy concentration being fixed in each of the deficient heterostructure models, we find varied behavior depending on the location of the vacancy. The vacancies in positions 1, 2, and 4 each decrease the magnetization to between 2.7-2.8 μ_B per Mn, see Fig. 3. The vacancy in position 3 results in a more considerable reduction of the magnetization to 2.2 μ_B per Mn. The excess electrons are expected to occupy the majority spin e_g orbitals of the Mn $4+$ ions, increasing the magnetization. However, the magnetization reduction is consistent with experimental observation **?**]. In Fig. S1, we find charge redistribution throughout the layers. For the vacancies near the interface, a low spin t_{2g} configuration is favored over the high spin e_g filling for some layers. For each of the cases, the surface layer takes a low-spin insulating configuration.

Looking at the layer-by-layer magnetization in Fig. 4(a), we find clear development of a magnetic dead layer near the LSMO surface for each of the heterostructure models, which is consistent with the insulating low spin configuration. Dead layers are known to reduce the overall magnetization and lead to the destruction of the magnetization below a critical thickness. The presence of dead layers in the simulations is consistent with the reduced magnetization that we found for vacancies in position 1, 2, and 4. The greater reduction of the magnetization seen in the position 3 case is correlated with a reduced magnetization in the bulk layers in addition to the surface dead layers. In both cases, the layers with reduced magnetization align with the low spin configurations caused by the electronic redistribution.

3.3. Electrostatic Potential and Electronic Reconstruction:

Dead layer formation is often understood within the polar catastrophe model, in which the charge from the surface moves to the interface to screen the interfacial dipole that is created due to the oxidation state mismatch of the cations across the interface. Here, we consider the layer-by-layer average oxidation state of the Mn cations, presented in Fig. 5 to gain further insight into the transfer of charge. In each of the thin films, we find that the oxidation state reduces from the nominal value of 3.3+ to between 2.8+ and 3.0+ in the bulk layers. Reduction at the interface is consistent with our prior work which demonstrated a reduction of the oxidation state to an approximate value of 2.5+ **?**], but the lesser reduction indicates that less charge is transferred to the interface in the presence of vacancies. The accumulation of charge at the interface is consistent with the polar catastrophe model in which charge moves to the interface in order to partially screen the dipole that arises from the valence mismatch with the Ti^{4+} cations. However, other experimental work demonstrates that oxygen vacancies are expected to cause the formation of Mn^{2+} cations **?**]. Looking at the intermediate layers, we also find a reduction in the oxidation state to between 3.0+ and 3.1+ which indicates accumulation of charge throughout the material in addition to the interface. In the polar catastrophe model, charge accumulation at the interface is compensated by the transfer of electrons away from the surface. Here, we find little to no oxidation at the surface layers, which indicates that the charge at the surface does not migrate in contrast with the expected behavior and in contrast with our prior work where we found that the surface oxidation state increased to around 3.7+ **?**

]. From this analysis, we find that the excess charge from the vacancies localizes near the interface but also redistributes throughout the material.

To gain insight into the redistribution of the excess charge, we calculated the macroscopic average of the local electrostatic potentials for each of the deficient films. The electrostatic potential shown in Fig. 6 has distinct behaviors across the interface between 17.5-21.8 Å, from the interface to the position of the vacancy, and from the vacancy to the bulk of the LSMO. In each of the thin film models, we find a potential gradient across the interface as expected from the polar mismatch. For the pristine heterostructure, the average change in the potential is 384 meV$\cdot$Å^{-1}. Introducing vacancies reduces the average change in potential across the interface to 364 meV$\cdot$Å^{-1} for the vacancy positioned farthest from the interface. The vacancy positioned immediately at the interface reduces the average change in potential to 287 meV$\cdot$Å^{-1}.

Although it is evident that excess charge from the vacancies reduces the interfacial dipole, it does not entirely prevent the field from entering the bulk layers of the LSMO. This can be seen in the behavior of the potential in the region spanning from the interface to the vacancy as well as in the region spanning from the vacancy to into the bulk of the LSMO. The potential takes a local maximum near the position of the vacancy in each of the cases. In contrast, the pristine case displays monotonic behavior over the same regions. From an electrostatic standpoint, the emergent potential barriers near the vacancy site are repulsive to nearby charges. This result is consistent with recent work that has indicated that vacancies may act as scattering centers that disrupt the flow and transfer of charge **?**]. The emergence of the scattering potentials prevents charge from transferring from the surface to the interface as we found with the oxidation state analysis. This leads to the charge redistribution that can be seen in the layer-by-layer DOS presented in Fig. S1, which is consistent with the reduction that we found for the oxidation states in the bulk layers. Since the double-exchange mechanism delicately depends on the Mn oxidation state **?**], the prevalence of $\mathrm{Mn}^{2.8+}$ - $\mathrm{Mn}^{3.1+}$ throughout the LSMO layers may lead to local spin flipping which could be responsible for the deterioration of magnetization seen throughout the heterostructure with the vacancy in position 3.

3.4. Local Properties in the Bulk Crystal:

To consider the local impact of the vacancies on the magnetic structure, we turn our attention to the bulk LSMO structure with varying degrees of oxygen deficiency looking to build an atomistic model that describes the magnetic consequences that may arise due to the redistribution of charge that results from the vacancies acting as scattering centers. To do so, we surveyed a landscape of oxygen-deficient LSMO structures. Starting from the pristine reference, we created oxygen-deficient $\mathrm{La}_{0.7}\mathrm{Sr}_{0.3}\mathrm{MnO}_{3-\delta}$ structures for $\delta = 0.125$, 0.250, keeping the La:Sr ratio fixed. In increasing order, the defect concentrations correspond to 1 vacancy per 40-atoms cell and 1 vacancy per 20-atoms cell. In the orthorhombic phase, LSMO has two independent oxygen lattice sites. Namely, oxygen may occupy the apical vertices of the coordination octahedra or the planar vertices. For $\delta = 0.125$ and 0.250, we created the two symmetry inequivalent vacancies by removing an apical oxygen and a planar oxygen, separately, to create the distinct structures as shown in Fig. 7(a).

Furthermore, we addressed the possible impact on the magnetic structure by considering type A-, C-, and G-AFM order as well as the FM state for each vacancy arrangement as defined schematically in Fig. 7(b). After optimization, we calculated the formation energy for each structural and magnetic configuration to understand the relative stability as detailed in Fig. 7(c). For $\delta = 0.125$, the apical site is more favorable than the planar site for each of the magnetic configurations. Although the FM configuration is the most energetically favorable, the type A-AFM configuration is nearly degenerate with an energy difference of 8 meV. Similarly, the type C-AFM apical site and the FM planar site have a difference of 20 and 24 meV, respectively. Comparatively, AFM order in the planar site and the type G-AFM order as a whole are unfavorable with energy differences greater than 50 meV. The close energy differences indicate that vacancies likely form in a mixture of these configurations in physical samples, and that vacancy formation may introduce local spin flipped sites. The $\delta = 0.250$ continues this trend, whereby the type A-AFM apical site is entirely favored with a formation energy of 1.07 eV. In this case, the FM order is unfavorable with an energy difference of 34 meV for the apical site and 70 meV for the planar site. Likewise, the planar site is unfavorable with differences ranging between 60-90 meV.

To better understand how the tendency towards spin flipping may be associated with the transfer of charge, we will focus on the lowest energy configuration for both the apical and planar vacancies for both concentrations. First looking into the electronic density of states (DOS) presented in Fig. 8. For apical vacancies with $\delta = 0.125$ shown in Fig. 8(a), the d_{z^2} states of the deficient Mn sites shift to lower energies as a result of the vertical square pyramidal coordination. The excess electrons from the vacancy formation can be seen to localize in the d_{z^2} states of the deficient Mn. In addition to the spin-up states, the vacancies introduce states into the spin-down channel at the Fermi level. The new spin down d_{z^2} states do not reflect the crystal field and can be seen clearly as dangling bonds in the charge density shown in Fig. S2. The $d_{x^2-y^2}$ states are affected to a lesser extent and remain at the Fermi level. However, the number of states near the Fermi level reduces for the vacant Mn. In particular, the depletion in available states just above the Fermi level coincides with an increase in the Fermi level states of the neighboring Mn.

The apical vacancies in the $\delta = 0.250$ structure shown in Fig. 8(b) demonstrate more splitting between the e_g states as seen by the complete separation of the d$_{z^2}$ and d$_{x^2-y^2}$ states near the Fermi level. As in the lower concentration, the broken bonds result in square pyramidal coordination of the vacant Mn. The d_{z^2} states now shift completely below the Fermi level. The d_{z^2} states form dangling bonds (see Fig. S3), as in the $\delta = 0.125$ concentration. The $d_{x^2-y^2}$ states remain at the Fermi level, but the number of states reduces considerably. The reduction coincides with an increase in the number of $d_{x^2-y^2}$ and d_{z^2} states for the neighboring Mn. Additionally, the shifts in the d_{z^2} states of the deficient Mn and the $d_{x^2-y^2}$ states of the neighboring Mn give rise to orbital ordering at the Fermi level as seen by the site-based occupation of either d$_z^2$ or d$_{x^2-y^2}$ at the Fermi level.

For the planar vacancies with $\delta = 0.125$ in Fig. 8(c), the extended planar bonds and horizontal square pyramidal coordination of the deficient Mn reduce the energy of the $d_{x^2-y^2}$ states and increase the energy of the d_{xy} states. Newly occupied spin-down $d_{x^2-y^2}$ and d_{xy} states emerge, indicating that the excess electrons from the vacancy formation localize on the deficient Mn ions. The local electronic structure of the neighboring Mn ions remains nearly identical to that of the pristine crystal.

For the planar vacancies with $\delta = 0.250$ in Fig. 8(d), the additional excess electrons due to the increased concentration of vacancies begin to fill the d_{z^2} states of the deficient Mn, reorganizing the electronic structure to accommodate type C-AFM order. The neighboring Mn ions now experience e_g splitting as a result of the sustained distortions. The d_{z^2} states are lower in energy as a result of the extended apical bonds with new spin-down states emerging.

The spatial effects significantly impact the electronic structure. The localization of dangling bonds and the distribution of the excess electrons influence the balance of the Mn^{3+} and Mn^{4+} states, affecting the magnetic structure. The charge transfer observed in both of the apical vacancy structures suggests that the mobile electrons may scatter from the dangling bonds.

By integrating the t_{2g} states up to the Fermi level and the e_g states from -4.0 eV to the Fermi level, we find that in each case the deficient Mn sites reduce to an oxidation state between 3.0+ and 3.1+. For the 0.125 structures, the rest of the Mn sites retain an average oxidation state of 3.3+. The non-deficient sites in the 0.250 structures reduce to an average of 3.15+. Given the tendency for the excess charge to localize near the vacancy and the reduction that we find in the Fermi level states of the deficient Mn sites, it is clear that the vacancies act as scattering centers as we found in the thin film models.

The evolution of the magnetic order can be understood by examining the magnetic exchange coupling between Mn atoms. In the pristine material, the FM state is driven by the double exchange mechanism. In Fig. 9(a) the exchange parameters of the pristine structure are relatively uniform and strongly ferromagnetic, reflecting the underlying mechanism. For $\delta = 0.125$ with apical vacancies, we find a weak AFM interaction directly across the broken bond. Additionally, the FM interactions between the deficient Mn and its neighbors weaken due to the reduced number of states near the Fermi level for the deficient sites. On the other hand, the interactions between Mn with completed octahedra remain strongly FM which is consistent with the prevalence of Mn$^{3.30+}$ away from the vacancy.

For the $\delta = 0.250$ concentration, the AFM interaction directly across the vacancy increases dramatically. The dangling bond state retains the spatial localization as in the lower concentration. In contrast, the fully spin-polarized states of the dangling bonds strengthen the interaction. The interaction across the apical bond of the vacant Mn is also strongly AFM. Since the deficient Mn retains $d_{x^2-y^2}$ states at the Fermi level, the electron from the neighboring Mn can hop to the deficient Mn. This hopping is prominent as the bonding network is broken along the c-axis, whereas the network is intact within the $a - b$ plane. To replace the hopped electron of the octahedral Mn, an electron can hop from a neighbor through a double exchange. As a result, the interactions between non-deficient Mn are strongly FM. The resultant magnetic exchange locally favors spin flipping along the c-axis, because the direct exchange across the vacancy is dominant and intralayer coupling in the a-b plane remains FM.

For the planar vacancies, the $d_{x^2-y^2}$ defect levels are fully localized even for the $\delta = 0.125$ structure, reducing the number of states near the Fermi level. This leads to a nearly vanishing FM interaction directly across the vacancy. On the other hand, the interaction across the remaining planar bonds becomes strongly AFM through the emerging super-exchange as a consequence of the lessened oxidation states of the deficient Mn. Away from the vacancy, the double exchange interactions dominate as the Mn^{3+} remains prevalent. Although the emergent super-exchange does not drive a complete magnetic transition, the overall FM interactions are weakened as the reduced oxidation state of the vacant Mn disrupts the electron hopping. The emergent super-exchange persists in the $\delta = 0.250$

structure. Due to the increased concentration, the structure is composed of alternating vacancy and vacancy-free layers along the c-axis. The alternating occupancy between these layers drives a weak FM double-exchange interaction for electron hopping along the c-axis. Conversely, the oxidation state of the intraplanar neighbors approaches $3.0+$ leading to the emergence of additional weak super-exchange in the intraplanar interactions. Since the deficient Mn retains d_{z^2} states at the Fermi level, the electron from the neighboring Mn can hop to the deficient Mn. This hopping is prominent as the bonding network is broken within the $a-b$ plane, whereas the network is intact along the c-axis. To replace the hopped electron of the octahedral Mn, an electron can hop from a neighbor through a double exchange. As a result, the interactions between non-deficient Mn are strongly FM. The resultant magnetic exchange locally favors spin flipping within the $a-b$ plane, because the super-exchange between deficient Mn is dominant and the coupling along the c-axis remains FM.

4. Conclusions and general remarks

In this work we examined, from theory, the impact of oxygen vacancies on the electronic and magnetic structure of LSMO thin films as deposited on top of $SrTiO_3$ (001). Although the formation of dead layers reduces the overall magnetization of thin films, further deterioration above the critical thickness where the magnetization vanishes can be associated with oxygen vacancy formation. Globally, we found that oxygen vacancies play a compensating role to partially screen the interfacial dipole. However, the tendency for the excess charge to localize near the vacancy sites in dangling bonds introduces scattering potentials that impede the transfer of charge from the surface according to the polar catastrophe model.

This leads to redistribution of charge that causes the Mn oxidation states to reduce throughout the bulk layers LSMO. Locally, we found that reduction away from the nominal $Mn^{3.3+}$ state due to the introduction of vacancies disrupts and weakens the FM double-exchange and introduces competing super-exchange interfaces due to the depletion of Fermi level states. These competing magnetic interactions favor local spin flipping, which is consistent with the further deterioration of the net magnetization that could be explained by surface dead layers.

5. Acknowledgements

We acknowledge Robbyn Trappen, Chih-Yeh Huang, Aubrey N. Penn and James LeBeau for fruitful discussions. We thank the Pittsburgh Supercomputer Center (Bridges2) and San Diego Supercomputer Center (Expanse) through allocation DMR140031 from the Advanced Cyberinfrastructure Coordination Ecosystem: Services & Support (ACCESS) program, which is supported by National Science Foundation grants #2138259, #2138286, #2138307, #2137603, and #2138296. We also recognize the computational resources provided by the WVU Research Computing Dolly Sods HPC cluster, which is funded in part by NSF OAC-2117575. The work by AHR and Z. Romestan was supported by the grant DE-SC0021375 funded by the U.S. Department of Energy, Office of Science. XH thanks the support of the EU H2020-NMBP-TO-IND-2018 project "INTERSECT" (Grant No. 814487). A.C.G.C. acknowledges the grant No. 4211 entitled “Búsqueda y estudio de nuevos compuestos antiperovskitas laminares con respuesta termoeléctrica mejorada para su uso en nuevas energías limpias” supported by the VIE – UIS. Additionally, ACGC also acknowledge the support from the GridUIS-2 experimental testbed, being developed under the Universidad Industrial de Santander

(SC3-UIS) High Performance and Scientific Computing Centre, development action with support from UIS Vicerrectoría de Investigación y Extension (VIE-UIS) and several UIS research groups as well as other funding resources. This work was performed in part at the Analytical Instrumentation Facility (AIF) at North Carolina State University, which is supported by the State of North Carolina and the National Science Foundation (award number ECCS-2025064). The AIF is a member of the North Carolina Research Triangle Nanotechnology Network (RTNN), a site in the National Nanotechnology Coordinated Infrastructure (NNCI). This material is based upon work supported by the National Science Foundation under Grant No. DGE-1633587. This work was partially funded in thanks to support provided by NASA EPSCoR Award #80NSSC22M0173.

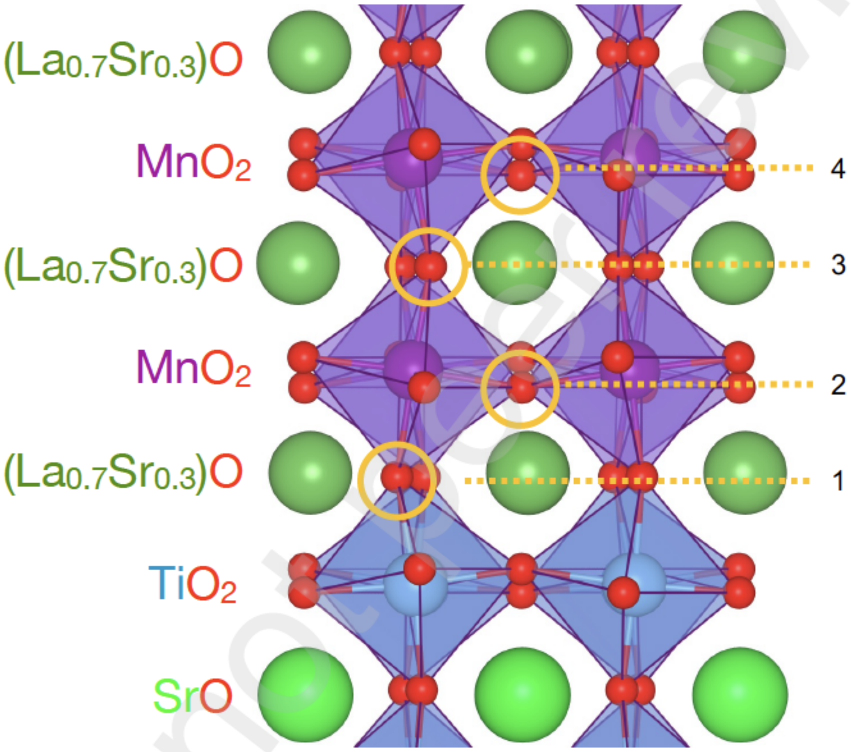

Figure 1: (Color online) **(a)** Pristine LSMO/STO heterostructure is shown near the interface with orange circles highlighting the four OV positions that were studied. The red atoms are O, the purple atoms are Mn, the blue atoms are Ti, the light green atoms are Sr, and the dark green atoms are the La/Sr pseudoatoms.

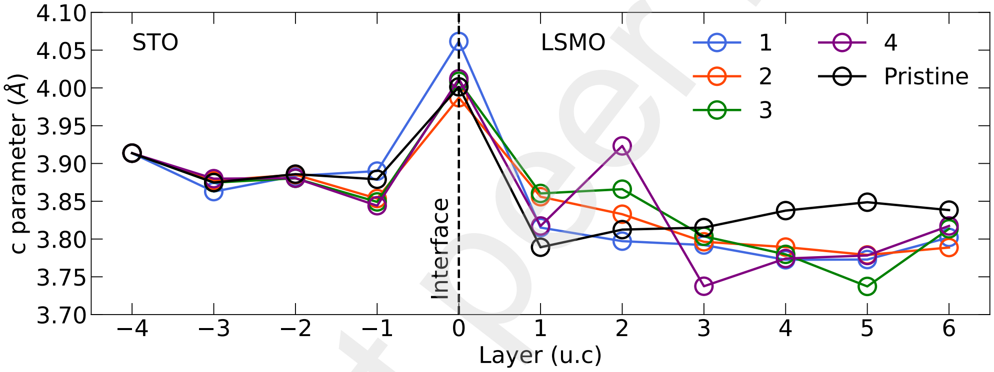

Figure 2: (Color online) Pseudocubic c lattice parameter for each layer of the four deficient heterostructures obtained theoretically. As ir can be noticed, the largest paramenter is observed at the interface potentially due to the strong electronic interactions.

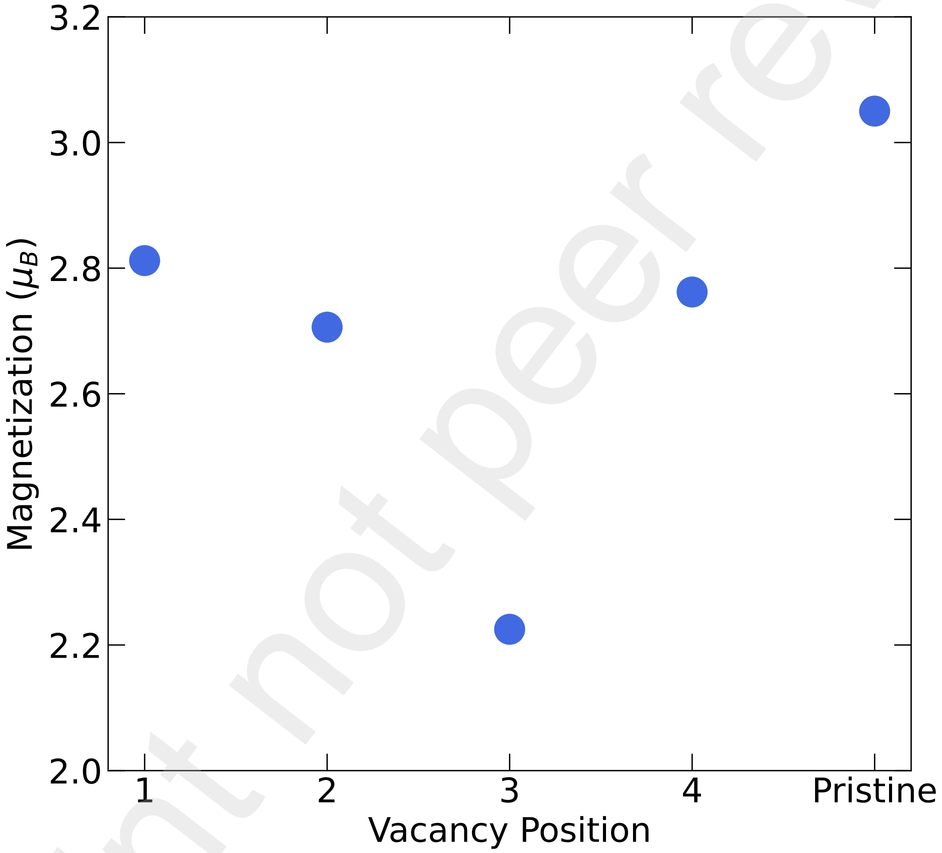

Figure 3: (Color online) The magnetization per Mn for the four vacancy thin film structures.

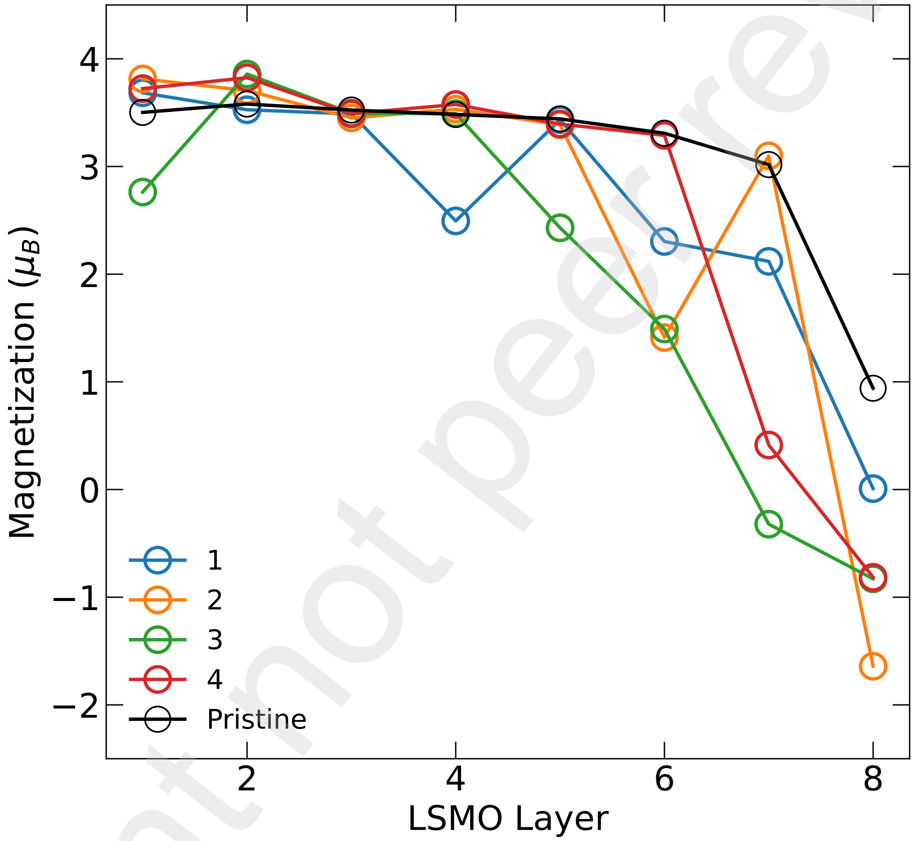

Figure 4: (Color online) Extracted magnetization per layer of the four deficient heterostructures. As observed, the magnetization consistently decreases towards the surface.

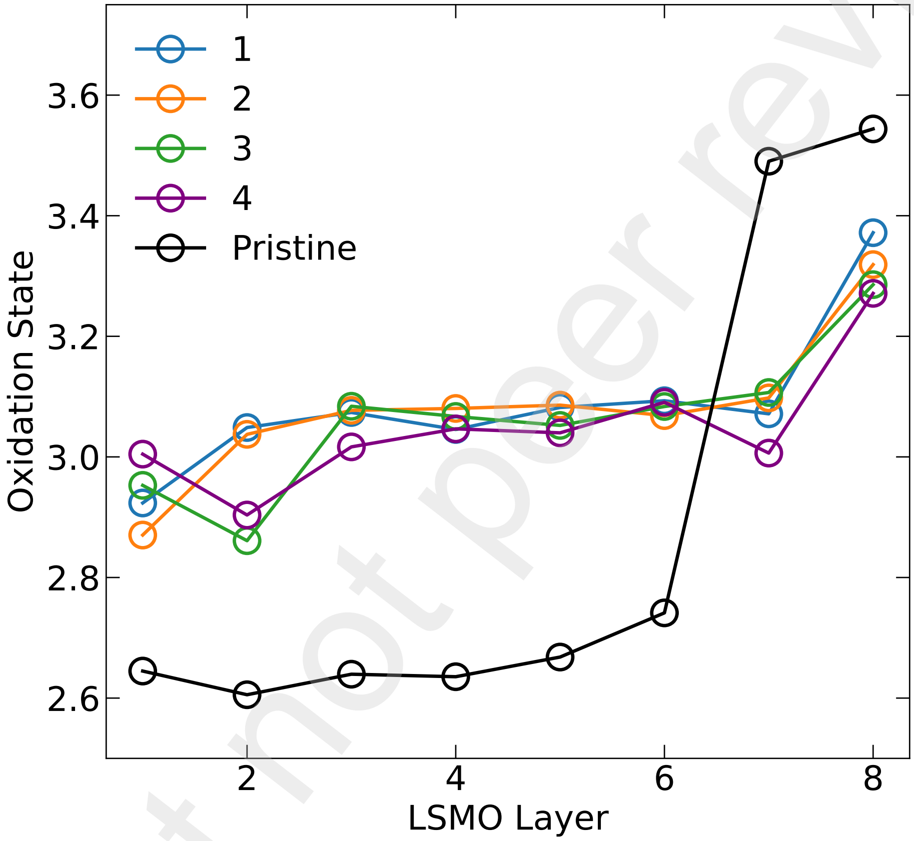

Figure 5: (Color online) Average oxidation state per layer of the four deficient heterostructures, computed via integrating the Mn t_{2g} states up to the Fermi level and the e_g states from -4 eV up to the Fermi level and subtracting the computed charge from the 7 valence electrons of the neutral Mn atom.

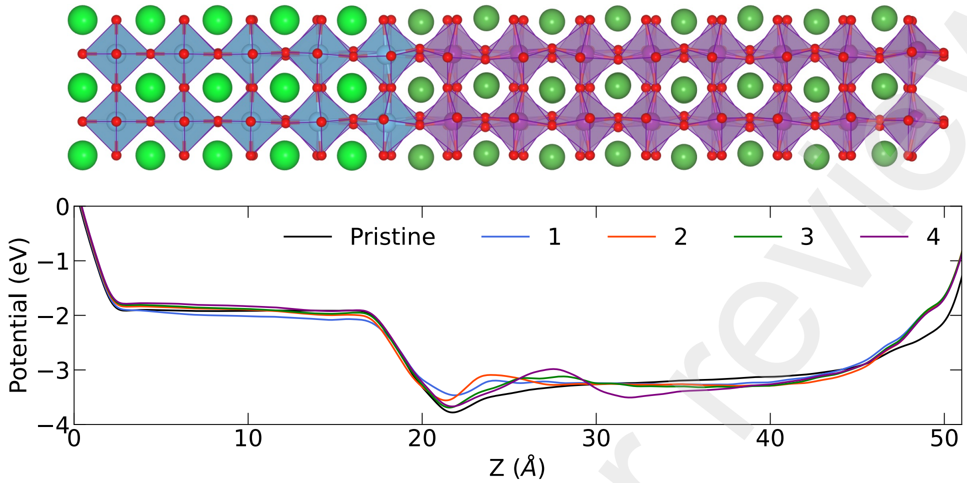

Figure 6: (Color online) Macroscopic average of the electrostatic potential in the four deficient heterostructures in comparison to that of the pristine heterostructure.

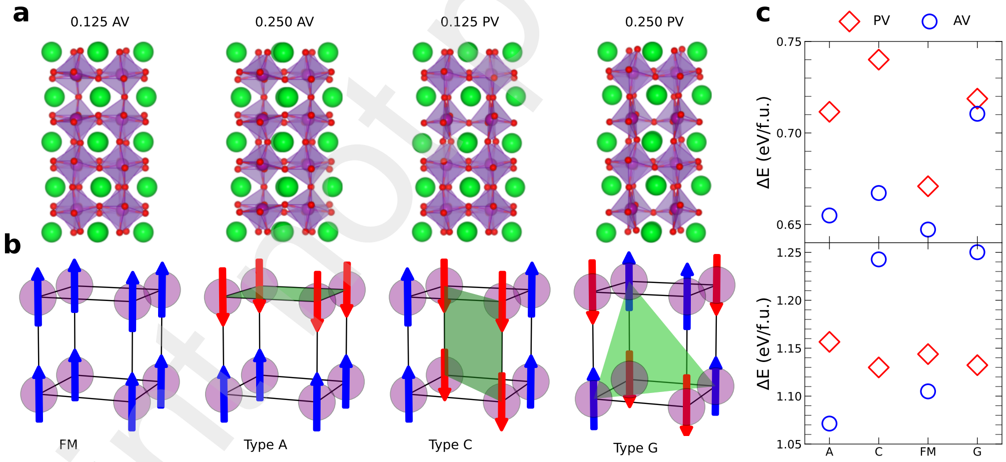

Figure 7: (Color online) OV can form either of the two Wyckoff positions for oxygen in the $Pnma$ unit cell of pristine LSMO, which are indicated by the highlights. The optimized structures for planar and apical vacancies where $\delta = 0.125$ and 0.250 are in (a). In **(b)**, The magnetic configurations are schematically defined over the Mn sub-lattice. The computed formation energies are shown in **(c)** for $\delta = 0.125$ (top) $\delta = 0.250$ (bottom).

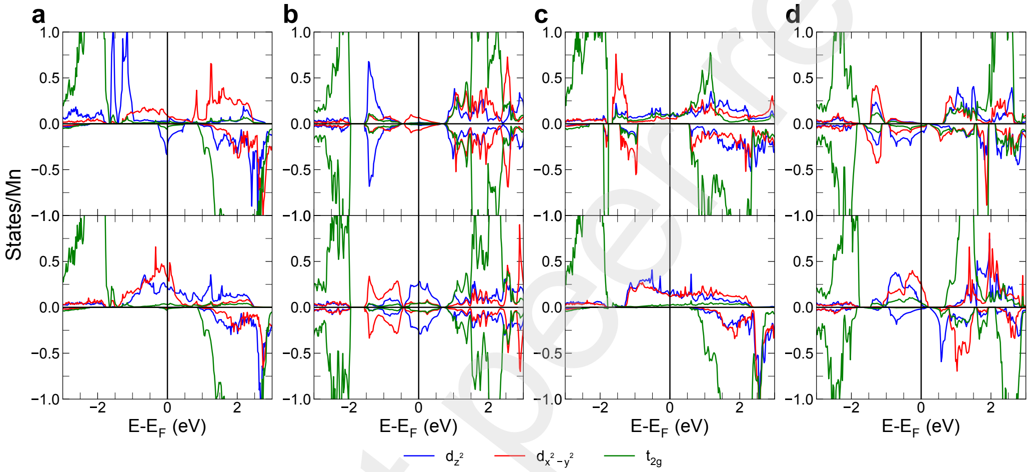

Figure 8: (Color online) Spin and d-orbital resolved density of states are shown for **(a)** $\delta = 0.125$ with apical vacancies, **(b)** $\delta = 0.250$ with apical vacancies, **(c)** $\delta = 0.125$ with planar vacancies, and **(d)** δ =0.250 with planar vacancies details. The top panels are for M$_{NN}$ to the vacancy, and the bottom panels are for Mn$_{NNN}$ to the vacancy. The changes in the electronic structure are a result of the structural distortions and additional electrons from the vacancy formation. In each plot, the positive counts indicate spin-up states, and the negative counts indicate spin-down states.

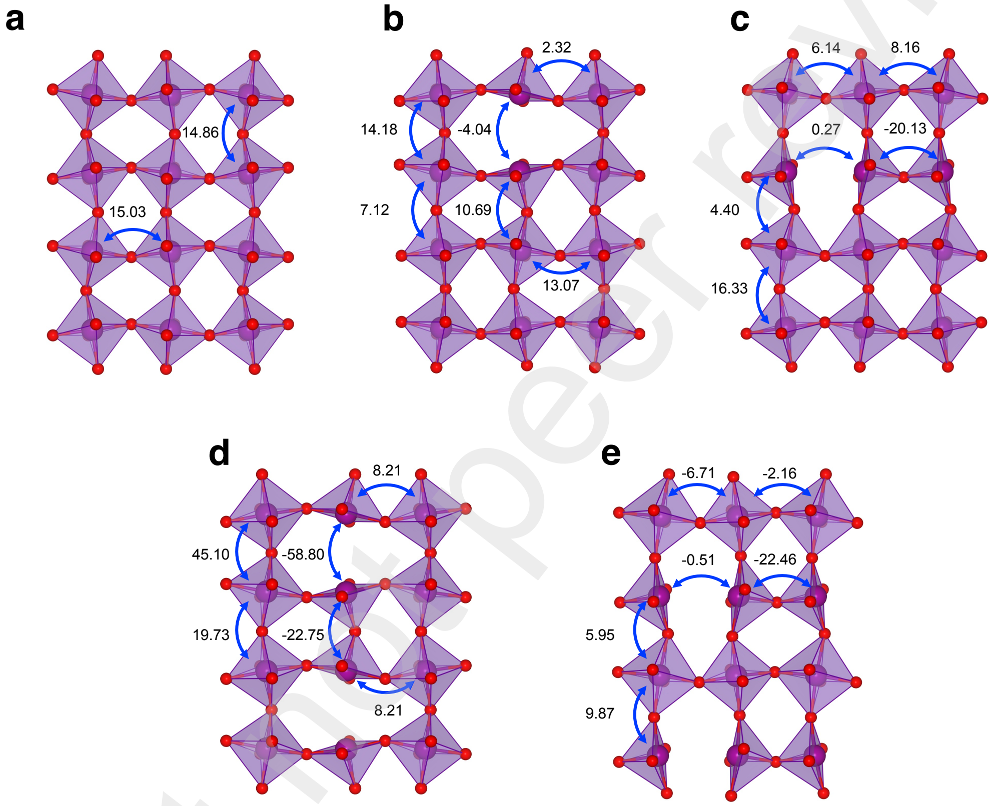

Figure 9: (Color online) The magnetic exchange parameters are presented schematically for **(a)** $\delta = 0$, **(b)** $\delta = 0.125$ with apical vacancies, **(c)** $\delta = 0.125$ with planar vacancies, **(d)** $\delta = 0.250$ with apical vacancies, and **(e)** $\delta = 0.250$ with planar vacancies in meV.